Laser and vision-based measurements of helicopter blade angles

Emanuele Zappa[1], Rui Liu[1*], Lorenzo Trainelli[2], Andrea Ferrario[1], Potito Cordisco[3], Mauro Terraneo[3], Riccardo Grassetti[4], Matteo Redaelli[5]

[1]Department of Mechanical Engineering, Politecnico di Milano, Milano, Italy

[2] Department of Aerospace Science and Technology, Politecnico di Milano, Milano, Italy

[3]Vicoter, Via Stoppani, Calolziocorte, Italy

[4]Logic, Cassina de' Pecchi, Italy

[5]Leonardo Helicopters, Cascina Costa di Samarate, Italy

Abstract

In this paper, three novel non-contact measurement systems for helicopter rotor blades, based on the 2D laser triangulation, the single camera and the stereo camera respectively, are designed and developed. The three measurement systems are applied to reconstruct the spatial position of the blade, and consequently its attitude angles. The measuring qualities of the three systems are assessed by means of experiments, including vibration tests, coupled rotation and vibration tests, and accuracy tests with complex motion configurations. These tests demonstrate that the three solutions can perform continuous operation correctly in a relevant dynamic environment. The results of accuracy tests show that, while all the systems can be successfully applied for the measurement of the angles of a helicopter blade, the stereo camera system provides a better accuracy than the other two systems. In particular, for the stereo camera system, the discrepancies of the three angles are comprised between 0.1 and 0.3 degrees in case of realistic blade motion conditions.

Keyword: angle measurement, 2D laser triangulation approach, vision-based approach, blade motion test, vibration test, rotation and vibration test

1. Introduction and state of the art

In modern helicopters, the interaction between fuselage and main rotor dynamics plays a crucial role in aircraft behavior. Aircrafts are nowadays equipped with a flight control system with the main goals to stabilize the vehicle, improve the comfort and reduce the pilot workload. The fuselage motion is one of the typical input of the flight control systems, while to date no operational rotorcraft is permanently fitted with equipment devoted to the real-time acquisition of blade motion, of either the main or tail rotor. The potential availability on board of a rotor state measurement system (i.e. a system capable of the instantaneous orientation of each blade) can be exploited to implement innovative rotor state feedback laws for attitude control augmentation [1][2]. Moreover, the rotary-wing vehicles operations are often limited by the admissible levels of external noise emitted, in particular in flying terminal procedures over

* Corresponding author.
E-mail address: rui.liu@polimi.it

densely inhabited areas. By measuring blade motion on the fly and using this information as an additional input for the flight control system, it could be possible to derive specific quantities to be used not only in the estimation of rotor (and hence vehicle) dynamics, but also in the prediction of radiated noise [3][4], vehicle closed-loop control laws [5][6], vehicle monitoring, or parameter identification [7]. Direct knowledge of rotor state can also be used to protect against envelope limits associated with flapping angles or hub moments [8].

The present contribution concerns the activities carried out in WP2 “Flapping measurement system preliminary studies” of the Clean Sky GRC5 MANOEUVRES project [9]. This work is focused on the design, implementation and testing of an innovative measuring device for the real time measurement of the main rotor tip-path plane (TPP) orientation with respect to the fuselage. This result is obtained measuring the blade motion (in particular the pitch, flap and lag angles, in the case of a fully articulated rotor) by means of contactless measuring devices installed on the rotor head.

The motion of the blade strongly depends on flight conditions [10][11], and changes dynamically during flight due to the combination of the relative motion imposed by the flight control system and the action of aerodynamic forces. Moreover, the centrifugal loading, the high vibration level prevailing on the rotor head and the strict constraint in terms of added mass and available space, make the development of a sensor system to be installed on rotor head extremely challenging.

In the scientific literature, contact-based sensors have been applied for blade angle measurement [12][13]. These sensors, such as potentiometer and rotary variable differential transformers are usually mounted directly on the blade [14][15]. However, for a long-term measurement task, there is a high risk of mechanical fatigue failure of the elements subjected to dynamic conditions. Due to this reason, contactless measurement techniques are targeted in this work in order to reduce the impact of mechanical fatigue on sensors and to boost the reliability of the system. Relying on these considerations, a set of potential contactless solutions have been selected, which appeared to potentially satisfy all relevant requests for blade angle measurements.

Ultrasonic sensors natively measure the linear displacements of a target, however it was demonstrated that they can be used for angular measurements as well [16][17]. Shoval and Borenstein [18] applied multiple ultrasonic sensors to measure the angular position of a mobile robot. Angular position can be measured also with capacitive [19][20] and magneto-inductive [21] sensors. However, in the technology review developed at the beginning of this work, ultrasonic, capacitive and magneto-inductive sensors were considered sub-optimal due to their potentially high sensitivity to environmental conditions such as presence of dirt, moisture, water, air turbulence.

Up to now, only a few scientific papers and patents describe the direct application of contactless measurement techniques on the measurement of the angle of the blade. Mandache [22] applied pulsed eddy current technology to measure the blade tip displacement of an aircraft turboengine. To overcome harsh working environment, Lai [23] developed an eddy current sensor with low temperature co-fired ceramics (LTCC) technology for blade tip timing systems. Hall effect sensors have also been proposed for rotor position determination in [24], while Buschbaum and Plassmeier [25] successfully applied Hall effect sensors for the flapping motion of the helicopter tail rotor in wind tunnel tests. Dimitrov [26] developed a 3D silicon Hall effect sensor for precise angular position measurements, potentially allowing to measure the three blade angles contemporarily. For helicopter blade angle measurement, there is a limiting factor because of the complex i.e. possibly large and highly coupled motion of the blade, which does not offer a

fixed reference direction for its displacements with respect to the rotating frame. This inspires to discard eddy current sensors due to their short measuring ranges and the inherent difficulties in measuring a 3D motion, in addition to a large measuring spot. Hall sensors are also rejected because they need an accurate, constant alignment with the target, which is a potentially problematic factor in blade angle estimation.

Other types of sensors that can be considered for measuring blade angles are laser-based and vision-based devices. All of them are popular in the measurement of the distance and the motion of an object [27][28]. Laser distance transducers can be employed to measure the flap, lag (or lead-lag) and feathering motions of the main rotor blades in flight [2][29]. An image-based approach is applied for tracking the helicopter TPP angle [30]. A stereo camera system is designed to estimate the position and the orientation of the blade in [31]. Vision sensors can realize a full-field measurement with high robustness, while 2D laser triangulation sensor, combining laser and camera techniques together, can realize long distance measurements [32][33]. The final outcome of the technology review was the choice of 2D laser triangulation sensor and vision sensor as promising candidates for the measurement of the angle of the blade.

This paper describes the design, implementation and testing of the solution proposed for the measurement of the rotor blade angles. The target vehicle chosen in the MANOEUVRES project is the AgustaWestland AW139, a medium lift helicopter equipped with a five-bladed, articulated main rotor. The MANOEUVRES project has been carried out by a consortium involving four partners (Politecnico di Milano, Università Roma Tre, Vicoter, and Logic), in close co-operation with Leonardo Helicopters that contributed with technical support and experimental resources. The overall goal of the project is to monitor rotorcraft noise in flight, in view of optimized noise-abatement terminal procedures. To achieve this goal, it is necessary to estimate the blade motion in real time [34], in order to derive TTP. This, in turn, can be related to the TPP angle of attack, which contributes primarily to the determination of the emitted noise together with airspeed and disk loading [35].

The measurement of the blade angles could be combined with the pressure distribution along the blade, estimated with a novel pressure and temperature sensitive pain and a monochrome camera [36][37]. The time-resolved surface pressure measurements generated by this type of measuring device, coupled with the measured blade motion can be useful to further develop the analysis of the unsteady aerodynamics of rotating blades.

The three solutions proposed in this work for blade angle measurement are described in section 2. The first technique, described in section 2.1, is based on the use of a 2D laser triangulation sensor, coupled with a proper 3D target. The second and third solutions are based on a single camera approach, as described in section 2.2, and on a stereo camera one, as described in section 2.3, respectively. Multiple experimental campaigns, including vibration tests, coupled rotation and vibration tests, and accuracy tests using real helicopter components have been conducted to evaluate the three solutions, as reported in section 3.

2 Measurement principles

In a typical helicopter main rotor, the motion of the blade root with respect to the hub is expressed by means of three angles: lag, flap and pitch. In Figure 1, a sketch of the main rotor topology is shown, together with the reference systems and symbols used in this work. An orthogonal coordinate system (X_f, Y_f, Z_f) fixed to the hub is applied to define the motion of the blade, centered at the blade root. The blade

is thought to be initially positioned in a radial position with respect to the mast. With reference to this initial position, the X_f axis lies along the blade span and points towards the tip of the blade, while the Z_f axis is aligned with the rotor mast and points downwards. The Y_f axis is orthogonal to X_f and Z_f. The blade movement is described in terms of a sequence of partial rotations, in a given sequence. In the present case, the first is a pitch motion about the X_f axis, the second is a flap motion about the pitched axis corresponding to Y_f in the initial position, and a lag motion about the pitched and flapped axis corresponding to Z_f in the initial position.

All the methods proposed in this work to measure the blade angles rely on the detection of features of a target placed on the blade root. The 3D coordinates of these features are measured by the sensor system using a different approach for each of the three solutions. The 3D position of one of these features expressed in the fixed reference frame is defined as P_f. When the three blade angles are equal to zero, we define the same coordinates as P_{f0} and it is possible to write

$$P_f = R_c(\xi, \beta, \theta) P_{f0} \qquad (1)$$

where the rotation matrix R_c appears,

$$R_c = \begin{bmatrix} \cos\xi\cos\beta & \cos\xi\sin\beta\sin\theta - \sin\xi\cos\theta & \cos\xi\sin\beta\sin\theta + \sin\xi\sin\theta \\ \sin\xi\cos\beta & \sin\xi\sin\beta\sin\theta + \cos\xi\cos\theta & \sin\xi\sin\beta\cos\theta - \cos\xi\sin\theta \\ -\sin\beta & \cos\beta\sin\theta & \cos\beta\cos\theta \end{bmatrix} \qquad (2)$$

In the previous equation, R_c is represented as the matrix composed by the sequence of the partial rotations by lag angle ξ, flap angle β and pitch angle θ.

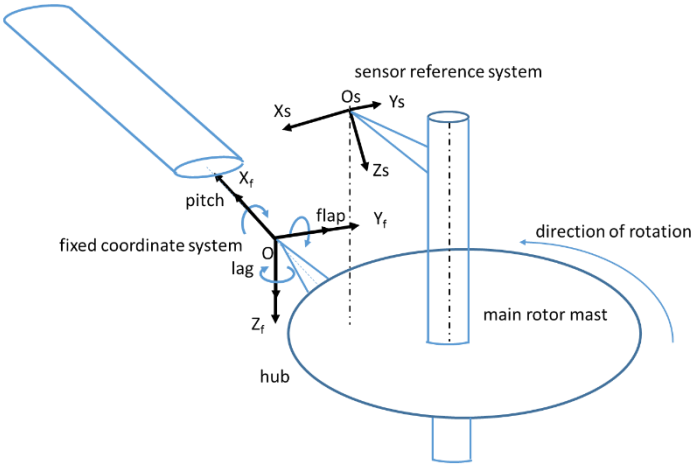

Figure 1: Sketch of the main rotor, reference systems and conventions.

As shown in Figure 1 and Figure 2, the sensor (either 2D laser or camera) is fixed on the hub and estimates the coordinates P_f with a procedure that depends on the sensor type, illustrated in the following. The coordinates P_{f0} are characteristics of the target mounted on the blade root and are estimated during the calibration of the measuring system, as described for each technique in the next sections. Since an adequate set of points P_{f0} is known from the calibration and the corresponding set of points P_f is measured, it is possible to estimate the R_c matrix using Eq. (1) and then the blade angles can be obtained using Eq. (2).

The target, designed with a geometrical shape that facilitates the feature detection by the sensor, is fixed on a body rigidly connected to the blade root, termed tension link. The tension link is connected to the hub by means of an elastomeric joint which realizes a spherical hinge.

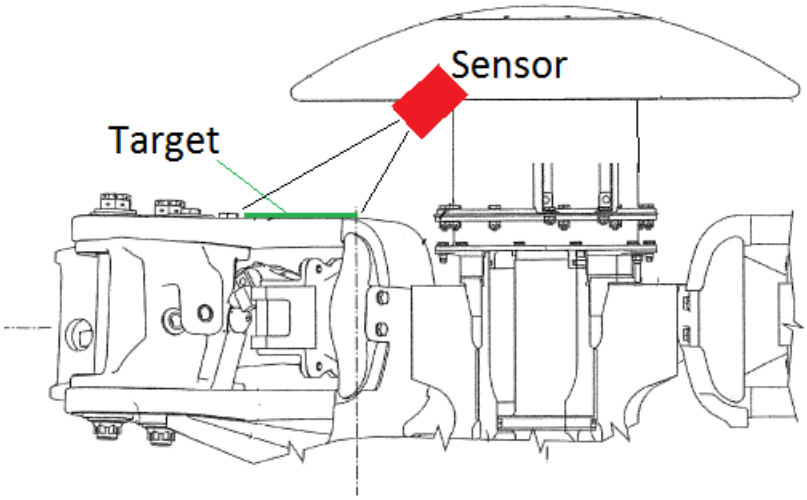

Figure 2: Arrangement of the measurement system (red) and target (green).

2.1 System based on 2D-laser sensor

Figure 3 shows the schematic diagram of the 2D-laser triangulation measurement system. For this solution, the target is designed to have a 3D shape with sharp corners, to allow an accurate feature detection with the laser. The laser plane is projected onto the surface of the target (Figure 3b). The profile of the intersection between the laser beam and the target is reconstructed in the laser coordinate system (Figure 3c). The corners (P_{L1} to P_{L9}) marked with a red cross are extracted by means of profile segmentation and local fitting technique [38].

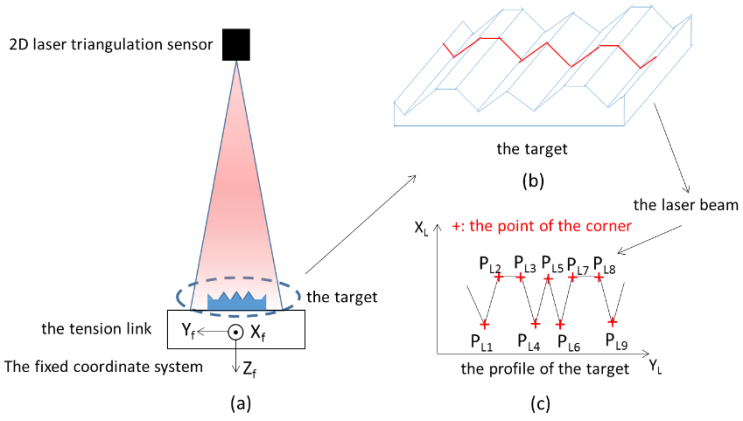

Figure 3: Measurement system based on 2D laser.

The 3D coordinates of the features (P_{L1} to P_{L9}) are detected in the laser sensor coordinate system (X_L,Y_L,Z_L), as seen in Figure 3, and are transformed in the hub-fixed coordinate system (P_{f1} to P_{f9}). Eq. (3) describes the transformation between the two coordinate systems.

$$P_f = R_L^{-1} P_L - T_L \qquad (3)$$

where

$$R_L = \begin{bmatrix} cos\alpha & 0 & sin\alpha \\ 0 & 1 & 0 \\ -sin\alpha & 0 & cos\alpha \end{bmatrix}, T_L = \begin{bmatrix} t_{Lx} \\ 0 \\ t_{Lz} \end{bmatrix} \text{ and } P_L = \begin{bmatrix} X_{L1} & \dots & X_{L9} \\ Y_{L1} & \dots & Y_{L9} \\ 0 & \dots & 0 \end{bmatrix}. \quad (4)$$

The transformation from fixed reference system to laser sensor reference system is composed of the rotation matrix R_L and translation matrix T_L. The parameters (α, t_{Lx}, t_{Lz}) of the transformation showed in Figure 4 are estimated by means of the calibration procedure described in the following.

Note that the Z_L coordinates of all points are null by definition, because the plane illuminated by the laser is defined by Z_L=0. The X_L and Y_L coordinates are obtained directly from the laser measurements.

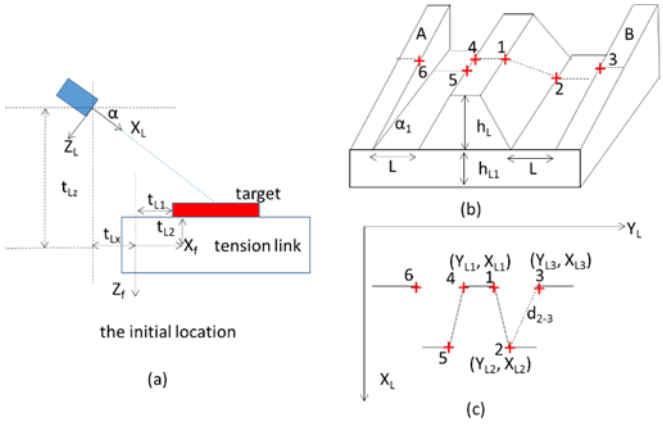

Figure 4: Laser-based solution calibration: conventions and symbols (a), calibration target (b) and features used in calibration (c).

In order to estimate the calibration parameters α, t_{Lx} and t_{Lz}, the blade must be set at the initial position (ξ=β=θ=0). Moreover, a different target is used for the calibration, because the target shown in Figure 3b used for the measurements is ambiguous for the translation along the X_L direction. The calibration target is shown in Figure 4b: the surfaces A and B are tilted of an angle α_1, as shown in Figure 4, to solve the ambiguity for the translation along the X_L direction. By the 2D triangulation laser sensor, the positions of three assigned points 1, 2 and 3 are extracted in the laser coordinate system as shown in Figure 4c. Since the shape of the target is known, the angle α and the translations t_{Lx} and t_{Lz} can be computed by means of the following equations:

$$\alpha = \arcsin\left(\frac{h_L}{|X_{L1} - X_{L2}|}\right) \quad (5)$$

$$t_{Lx} = X_{L3}\cos\alpha - \sqrt{d_{2-3}^2 - L^2} \cdot \sin\alpha \cdot (tg\alpha_1)^{-1} - t_{L1} \quad (6)$$

$$d_{2-3}^2 = (X_{L2} - X_{L3})^2 + (Y_{L2} - Y_{L3})^2 \quad (7)$$

$$t_{Lz} = X_{L2}\sin\alpha + h_{L1} + t_{L2} \quad (8)$$

where t_{L1}, t_{L2}, h_L, h_{L1} and L are known parameters from the layout of the calibration setup of Figure 4a.

Eqs. (5-8) deal with points 1 to 3 (Figure 4c) and allow to estimate the calibration parameters α, t_{Lx} and t_{Lz}. Since the calibration target is symmetric, an analogous procedure can be applied also for points 4, 5 and 6 (symmetric to 1, 2, 3) to obtain another estimate of the calibration parameters. Averaging the parameters obtained from the two estimates, a lower uncertainty on parameter estimation can be obtained.

As soon as the calibration parameters are estimated, the calibration target is removed and the measuring one (Figure 3) is mounted on the tension link. In order to recover the angles of the blade it is necessary to estimate which is the point P_{f0} that corresponds to the point P_f that we are currently measuring, but with the blade in reference position ($\xi=\beta=\theta=0$). The coordinates Y_{f0} and Z_{f0} of P_{f0} are known by means of the configuration of the setup, while X_{f0} has to be estimated. X_{f0} is not known because of the target ambiguity (target geometry does not change along the X_f direction). To estimate X_{f0} we can rely on the information that the blade rotates around the point OR_f (Figure 5), therefore we know that the distance d_f from P_f to OR_f is equal to the distance d_{f0} from P_{f0} to OR_f. The distance d_f is computed using the coordinates of the point P_f obtained in step 4, therefore the coordinate X_{f0} can be estimated imposing $d_f=d_{f0}$: at this point the three coordinates of the point P_{f0} are known.

The following points summarize the procedure for the system calibration and for the measurement of the blade angles in the case of the 2D laser solution:

1. Apply the calibration method to obtain the parameters α, t_{Lx}, t_{Lz}.
2. Acquire the profile of the target (Figure 3c) during the motion of the blade.
3. Detect the points P_L (L=1 to 9) in the laser coordinate system as shown in Figure 3c.
4. Apply Eq. (3) to convert the coordinates P_L of the points (measured in laser reference system) into the coordinates P_f (expressed in fixed coordinate system).
5. Estimate the coordinates P_{f0} corresponding to the coordinates P_f.
6. Insert the position P_f and P_{f0} into Eq. (1). The three angles are obtained by applying the pseudoinverse algorithm [39].

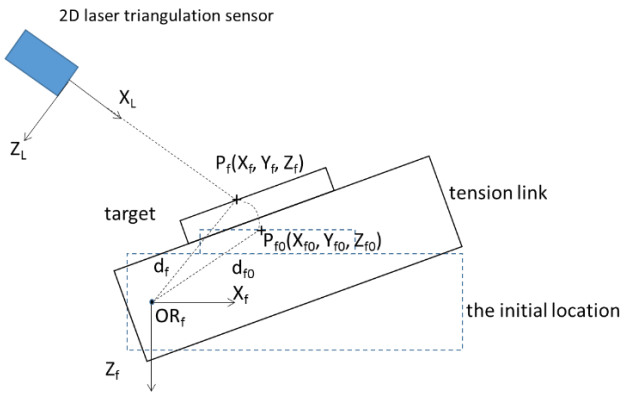

Figure 5: Location of the target during the motion of the tension link.

In the implementation of this measuring solution, the selected laser sensor was the Microepsilon 2650-100. This sensor was chosen because of its compact size, the capability to cover the needed measuring field and the possibility to obtain output data in a digital format compatible with a future transmission using a slipring for the communication from the sensor on the rotor head to the control PC hosted in the

helicopter fuselage. The scan rate is up to 40 Hz. The calibration and the measurement target were designed with a 3D CAD system and manufactured with a commercial 3D printer.

2.2 System based on single camera

The solution based on a single camera is shown in Figure 6. In this case, the target is a flat white sticker with 8 black blobs arranged on a regular grid. The thickness of the sticker can be neglected. The camera acquires the image of the target during the motion of the blade and, by means of blob analysis, the spatial position of the centroids of the blobs are estimated. Since the camera was previously calibrated [28], the relative position between the camera reference system and the hub reference system is estimated during the system setup (section 2.2.1), and the target geometry is known by construction, it is possible to apply a pose estimation algorithm [40] to the centroid coordinates to recover the spatial positions and orientation of the target (section 2.2.2). In this way, the 3D coordinates of the centroids of the blobs (Xsc,Ysc,Zsc) are recovered in the camera reference system.

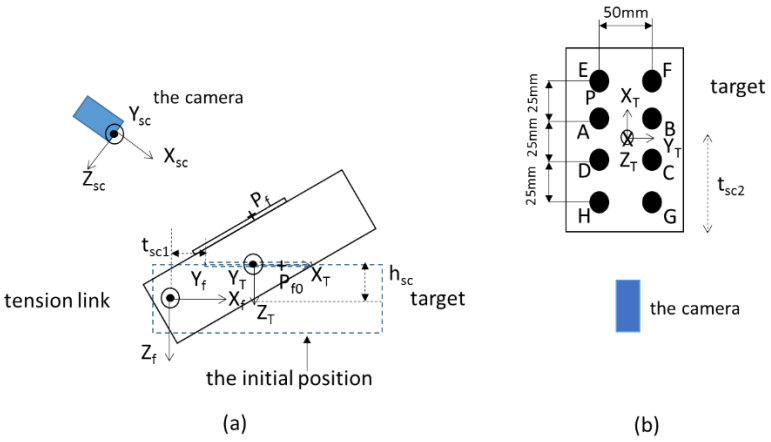

Figure 6: The measurement system based on single camera.

In both system calibration and angle measurement, the centroids of the blobs are extracted and sorted into a predefined conventional order, from A to H (see Figure 6). For the pose estimation, at least 4 of these blobs are necessary. Note that the larger is the target, the better is the expected accuracy in the angle estimation. Due to this reason, and since in the most of the physically possible blade orientation all the blobs are in the field of view of the camera, the set composed by E, F, G and H is usually selected for the measurement. In the event that one or more of the 8 blobs are out of the field of view of the camera, the processing software automatically selects the set composed by A, B, C and D instead. The measuring procedure is exactly the same for both the set of blobs; in the following of the discussion, the case of blobs E, F, G, and H is used.

As shown in Figure 6, three different coordinate systems are employed: the camera coordinate system (X_{sc}-Y_{sc}-Z_{sc}), the target coordinate system (X_T-Y_T-Z_T) and the hub-fixed coordinate system (X_f-Y_f-Z_f). In order to estimate the angle of the blade with respect to the hub, it is necessary to estimate the 3D coordinates of the blobs in the hub-fixed coordinate system. To this purpose, we can define the following transformations:

$$\begin{bmatrix} X_{sc} \\ Y_{sc} \\ Z_{sc} \end{bmatrix} = R_1 \begin{bmatrix} X_T \\ Y_T \\ Z_T \end{bmatrix} + T_1, \quad \begin{bmatrix} X_T \\ Y_T \\ Z_T \end{bmatrix} = R_2 \begin{bmatrix} X_f \\ Y_f \\ Z_f \end{bmatrix} + T_2 \qquad (9)$$

where R_1 and T_1 describes the transformation between the camera coordinate system and the target coordinate system, while R_2 and T_2 describes the transformation between the target coordinate system and the hub-fixed coordinate system. The numerical values of R_1, T_1, R_2 and T_2 are estimated during the system calibration.

2.2.1 Single camera system calibration

The goal of the calibration of the setup is to estimate the matrixes R_1, T_1, R_2 and T_2. For the calibration procedure, the blade is placed in the initial position (ξ=β=θ=0) and the position of the centroids of the blobs E, F, G and H are estimated. The matrix R_1 is then defined as:

$$R_1 = [v_1^{sc} \quad v_2^{sc} \quad v_3^{sc}]^T \qquad (10)$$

where v^{sc}_1 is the unit vector of the X_T axes expressed in the camera coordinate system and named X^{sc}_T, and analogously v^{sc}_2 and v^{sc}_3 are the unit vectors of Y_T and Z_T expressed in the camera coordinate system and named Y^{sc}_T and Z^{sc}_T respectively (see Figure 7).

The unit vectors v^{sc}_1, v^{sc}_2, v^{sc}_3, are estimated relying on the coordinates of the centroids of the 4 blobs in the camera system, as follows:

$$v_1^{sc} = \frac{\overline{E}^{sc} - \overline{H}^{sc}}{||\overline{E}^{sc} - \overline{H}^{sc}||} \qquad (11)$$

where $\overline{E}^{sc}$ represents the position of the center of gravity of the two blobs E^{sc} and F^{sc}, while $\overline{H}^{sc}$ represents the position of the center of gravity of the two blobs H^{sc} and G^{sc} (see Figure 7).

The unit vector v^{sc}_3 is determined as the direction orthogonal to the plane based on the four coplanar blobs (E, F, G, H). Finally v^{sc}_2 is determined by the cross product of v^{sc}_3 and v^{sc}_1. Note that the spatial position of all these blobs in the camera coordinate system has been obtained by means of the pose estimation algorithm.

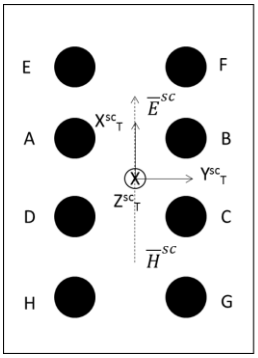

Figure 7: Calculation of the target coordinates in the single camera coordinate system.

Obviously, the rotation matrix R_2 between the target coordinate system and the fixed coordinate system is determined according to the layout of the setup, as shown by the following formula:

$$R_2 = \begin{bmatrix} 1 & 0 & 0 \\ 0 & 1 & 0 \\ 0 & 0 & 1 \end{bmatrix} \qquad (12)$$

Therefore, in the calibration, the rotation matrix R_{sc} between the camera coordinate system and the fixed coordinate system is determined by

$$R_{sc} = R_1 R_2 = R_1 \qquad (13)$$

The translation matrix T_{sc} between the camera coordinate system and the fixed coordinate system is determined by

$$T_{sc} = P_{f0} - R_{sc}^{-1} P_{sc0} \qquad (14)$$

where P_{f0} represents the position of the centroids of the blobs at the initial position (ξ=β=θ=0) in the fixed coordinate system. The coordinates P_{f0} are known by construction, since they depend on the pattern geometry and on the layout of the setup. P_{sc0} represents the position of the centroids of the blobs at the initial position (ξ=β=θ=0) in the camera system. P_{sc0} is determined by means of the pose estimation algorithm during the calibration.

After the calibration, the parameters R_{sc} and T_{sc} are estimated. Therefore during the measurement, the current positions of the blobs can be expressed in the fixed coordinate system.

2.2.2 Single camera system measuring technique

The pose estimation technique implemented for blade angles estimation is based on the technique proposed in [40]. The implementation for this specific application is described here. The blobs E, F, G, H (Figure 7) are used in the description of the technique but the implementation is the same if the blobs A, B, C and D are used. By construction of the target, it is known that the distance between blobs E and F is the same as the distance between blobs G and H. Therefore it is possible to write:

$$\overrightarrow{EF^{sc}} = \overrightarrow{HG^{sc}} \qquad (15)$$

or, explicitly,

$$\begin{bmatrix} X_F^{sc} - X_E^{sc} \\ Y_F^{sc} - Y_E^{sc} \\ Z_F^{sc} - Z_E^{sc} \end{bmatrix} = \begin{bmatrix} X_G^{sc} - X_H^{sc} \\ Y_G^{sc} - Y_H^{sc} \\ Z_G^{sc} - Z_H^{sc} \end{bmatrix} \qquad (16)$$

where C^{SC}_i (with C=X, Y and Z) are the 3D coordinates of the i^{th} point in camera reference system. The pinhole camera model, described in [28] and represented by the following equations,

$$\begin{cases} y = \frac{x}{f_u}(u - u_0) \\ z = \frac{x}{f_v}(v - v_0) \end{cases} \qquad (17)$$

is used here to analyze the image formation problem, while optical aberrations are previously compensated for, thanks to the camera calibration [28].

In Eq. (17) u_0 and v_0 are the pixel coordinates of the principal point, while f_u and f_v are the focal length in pixels. The four parameters u_0, v_0, f_u and f_v are obtained by means of the camera calibration. u and v are

the centroid of a blob in the image. The coordinates x, y, z are the spatial coordinate of the same blob in the camera coordinate system.

The coordinates of the blobs are then normalized dividing them by X_E^{SC}, as follows:

$$X_E^{sc\prime} = \frac{X_E^{sc}}{X_E^{sc}} = 1 \quad X_F^{sc\prime} = \frac{X_F^{sc}}{X_E^{sc}} \quad X_G^{sc\prime} = \frac{X_G^{sc}}{X_E^{sc}} \quad X_H^{sc\prime} = \frac{X_H^{sc}}{X_E^{sc}} \qquad (18)$$

Eqs. (16-18) can be combined into the following equation,

$$\begin{bmatrix} u_F & -u_G & u_H \\ v_F & -v_G & v_H \\ -1 & 1 & -1 \end{bmatrix} \begin{bmatrix} X_F^{sc\prime} \\ X_G^{sc\prime} \\ X_H^{sc\prime} \end{bmatrix} = \begin{bmatrix} u_E \\ v_E \\ 1 \end{bmatrix} \qquad (19)$$

Solving Eqs. (17) and (19) the coordinates $(X_E^{sc\prime}, Y_E^{sc\prime}, Z_E^{sc\prime})$, $(X_F^{sc\prime}, Y_F^{sc\prime}, Z_F^{sc\prime})$, $(X_G^{sc\prime}, Y_G^{sc\prime}, Z_G^{sc\prime})$, $(X_H^{sc\prime}, Y_H^{sc\prime}, Z_H^{sc\prime})$ can be obtained. According to the scaling introduced in eq. (18), eq. (20) can be written:

$$\overrightarrow{EF^{sc}} : \overrightarrow{E'F'^{sc}} = X_E^{sc} : X_E^{sc\prime} \qquad (20)$$

Then X^{sc}_E is solved. By means of inserting X^{sc}_E into Eq. (17), Y^{sc}_E and Z^{sc}_E can be obtained. Therefore, the coordinate of the blob E in the camera reference system is obtained. The coordinate of the other blobs F, G and H in the camera system are obtained with the same procedure.

Since the centroids of the blobs in the camera reference system are obtained by means of the pose estimation technique described above, the centroids of the blobs are further converted into the positions in the fixed coordinate system by means of the calibration parameters (see section 2.2.1). The centroids in the fixed coordinate system are finally inserted in Eq. (1) and the angle of the blade can be recovered.

The following points summarize the procedure for the system calibration and for the measurement of the blade angles in the case of single camera solution:

1. Apply the two-step calibration method to obtain the parameters R_{sc} and T_{sc} of the transformation between the camera coordinate system and the fixed coordinate system.
2. Acquire the images during the motion of the blade.
3. Extract the centroids of the 4 blobs in the 2D images.
4. Obtain the spatial position of the centroids of the blobs in the camera coordinate system by means of the pose estimation algorithm.
5. Compute the current positions $\mathrm{P_f}$ of the centroids of the blobs in the fixed reference system by the calibration parameters R_{sc} and T_{sc}.
6. Insert the current positions $\mathrm{P_f}$ and the known initial positions $\mathrm{P_{f0}}$ into Eq. (1). The three angles are obtained by applying the pseudoinverse algorithm.

In the implementation of single camera measuring solution, the selected smart camera was a Teledyne Dalsa BOA200 PRO. This camera was chosen because of its compact size (approximately a cube with 44 mm side) and the capability to process the images on board, by applying a user defined software in real time, and to generate a digital output compatible with a future transmission using a slipring, as in the case of the 2D laser solution. The focal length of the optics is 4.5 mm. The resolution of the image is 640 × 480 px and the frequency of the image acquisition is up to 35 Hz.

2.3 System based on stereo cameras

The solution based on stereoscopic cameras is schematically shown in Figure 8. The layout of the setup is similar to the case of the single camera. The main difference is that the 3D coordinates of the centroid of each blob is obtained here by means of stereo triangulation [41].

When the stereoscopic system is calibrated, the rigid displacement between the two cameras is estimated. Then, without loss of generality, the coordinates of the centroids (X_{LC},Y_{LC},Z_{LC}) are expressed in the left camera reference system. The target for stereo system is the same as the one for single camera: this choice allowed using both the measuring devices contemporarily during qualification tests and comparing easily the uncertainty associated to each of them in the same conditions.

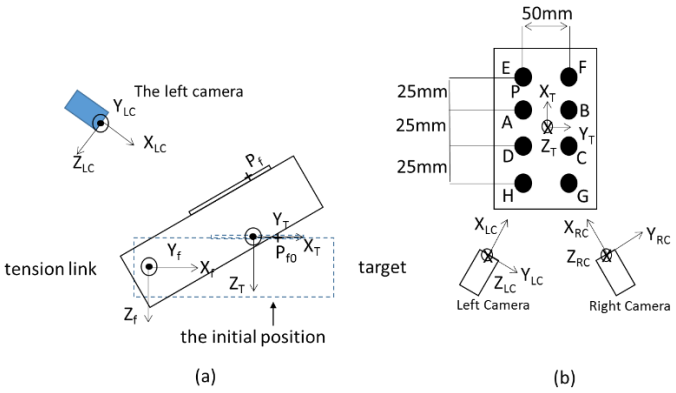

Figure 8: The measurement system based on stereo camera.

As shown in Figure 8, three coordinate systems are employed, as in the single camera solution: the left camera coordinate system (X_{LC},Y_{LC},Z_{LC}), the target coordinate system (X_T,Y_T,Z_T) and the hub-fixed coordinate system (X_f,Y_f,Z_f). The parameters of the transformation between the left camera reference system and the fixed reference system are obtained by means of a system calibration procedure, analogous to the one used for single camera solution.

Once the transformation between the camera reference system and the fixed reference system is obtained by means of system calibration, it is possible to estimate the position of the centroids of the blobs in the fixed coordinate system.

The following points summarize the procedure for the system calibration and for the measurement of the blade angles in the case of stereo camera solution:

1. Apply the calibration method to obtain the parameters of the transformation between the camera coordinate system and the fixed coordinate system.
2. Acquire the images of the target during the motion of the blade with the stereoscopic system.
3. Extract the centroids of the blobs (A to H) in each image.
4. Obtain the spatial position of the centroids of the blobs in the camera coordinate system by means of stereo triangulation.
5. Compute the current positions $\mathrm{P_f}$ of the centroids of the blobs in the fixed coordinate system.
6. Insert the current positions $\mathrm{P_f}$ and the known initial positions $\mathrm{P_{f0}}$ into Eq. (1) and apply the pseudoinverse algorithm to estimate the three angles of the blade.

In the implementation of stereo camera measuring solution, the selected cameras were a pair of AVT Marlin F131b, equipped with 1.2 Mpixel COMS sensor. The cameras were operated in partial scan with a resolution of 780 × 412 px in order to ensure a grabbing frequency of 35 Hz. The focal length of the optics is 4.5 mm to ensure the required field of view. These cameras were selected to reduce the hardware costs in the preliminary testing activity of the MANOEUVRES project, but may be substituted by smart cameras with onboard image processing capabilities in a future implementation. In particular it will be possible to consider the Teledyne Dalsa BOA200 PRO smart camera used in the single camera solution.

3 Experimental setup for measuring system validation

The three measuring solutions described in the previous sections represented the competing candidates for the final development within the MANOEUVRES project. In order to evaluate the most promising solution, an extensive experimental campaign was carried out on full-scale prototypal realizations of the three systems. This campaign involved test rigs at both the Politecnico di Milano and Leonardo Helicopters laboratories, and was structured on three types of tests, aimed at the verification of transducer functionality and actual capability in representative operating conditions. These tests, for which specific test beds have been developed, were the following:

1. Vibration tests: shakers driven by vibration spectra equivalent to the one measured in a real AW139 helicopter were employed, to test the ability of the prototype measuring systems to measure in realistic vibration conditions.
2. Coupled rotation and vibration tests: an A109MKII ironbird was used, i.e. a highly representative rotating rig, available at Politecnico di Milano laboratories [42], to validate the measuring devices considering realistic conditions in terms of centrifugal acceleration and gearbox-generated vibrations.
3. Accuracy tests: these were performed on multiple devices, including a complex, fully-coupled blade motion rig for the AW139 available at the Leonardo Helicopters laboratories, and allowed testing the measurement accuracy in the actual geometrical configuration envisaged for the target helicopter application.

Within this in-depth experimental analysis, all the necessary information in order to define the best solution for blade angle measurement was gathered. The extensive testing activity mentioned above allowed fully qualifying the candidate solutions. Some of the most relevant results are presented in the following sections.

3.1 Vibration tests setup

Vibration tests were aimed at the verification of the ability of the prototype measuring systems to work in realistic operating conditions with respect to vibrations. In these tests, the laser and cameras have been mounted on an electro-mechanical shaker driven with vibration spectra reproducing the operational vibration level measured in flight on an AgustaWestland AW139 main rotor hub (Figure 9).

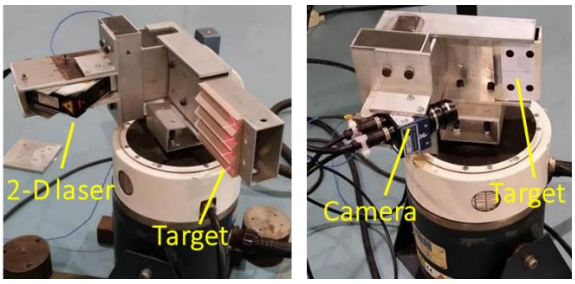

Figure 9: Vibration tests rig at Politecnico di Milano laboratories.

3.2 Coupled rotation and vibration tests setup

In coupled rotation and vibration tests, an A109MKII ironbird was employed (Figure 10). This equipment is basically a ground-tied helicopter fuselage complete with the original transmission gearbox and a simplified rotor head, driven by electric motors in place of the original turboshafts and capable of reproducing the AW139 main rotor speed. The laser and cameras have been fixed on the rotor head.

A109MKII ironbird at the Politecnico di Milano laboratories

Rotor head arrangement for 2-D laser system testing

Figure 10: The A109MKII ironbird used for coupled rotation and vibration tests at Politecnico di Milano laboratories.

3.3 Accuracy tests setup

Accuracy tests were mainly performed on the AW139 endurance rig at the Leonardo Helicopters laboratories. This rig is composed of a sub-assembly of the AW139 helicopter main rotor components. These tests allowed assessing the measuring system capabilities in acquiring blade motion, either moving the blade about one axis at a time, or in arbitrarily coupled lagging/flapping/ pitching conditions. Moreover, the endurance rig also allows to reproduce time histories acquired in flight of a complex continuous motion, fully coupling lag/flap/pitch blade angles. The test rig retrieves a reference measurement of the imposed angles with 247 Hz data acquisition, so that the measurement of the three different systems can be compared with the reference data. The sampling frequency of 247 Hz corresponds to 50 samples per revolution at the nominal rotation speed of the AW139 helicopter main rotor (4.94 rev/s). During flight, the helicopter blades show a strong dynamics related to the first harmonics of the main rotor rotation frequency. Due to this reason, the endurance rig used in these tests can impose mean angles, as well as the amplitude and the phase of the first three harmonics. All these parameters can be set by the user.

To understand the comprehensive capability of the three systems, different types of motion have been simulated during the tests, including pure lag, or flap, or pitch motion, combined lag/flap/pitch motion with different harmonic contents, and finally realistic blade motions corresponding to specific flight conditions. For the sake of brevity, only a small subset of the results of this extensive activity is shown in this paper. In particular, the cases of realistic blade motion corresponding to four different trimmed level

flight conditions at increasing airspeed values v_1, v_2, v_3 and v_4 (the actual airspeed values are not shown because of confidentiality obligations). During the tests, the range of explored angles spanned from -3.5° to 6° for the lag angle, from -2° to 12° for the flap angle and from -22° to 22° for the pitch angle.

4 Experimental results

4.1 Vibration tests and coupled rotation and vibration tests

In the vibration tests, the three systems correctly performed continuous operations, while acquisition and data transfer were not affected by such sustained vibration levels. Also in the coupled rotation and vibration tests, the three systems correctly performed continuous operations without any loss of data.

4.2 Accuracy tests: 2D laser triangulation system

Figure 11 shows one segment of the time history of lag/flap/pitch angles by means of 2D laser triangulation system, for the four different airspeed conditions v_1, v_2, v_3 and v_4, respectively. The blue curve represents the reference data and the red curve represents the data measured by the 2D laser system. The maximum discrepancy for the lag angle amounts to 1°, being fairly larger than the discrepancy for the flap and pitch angles.

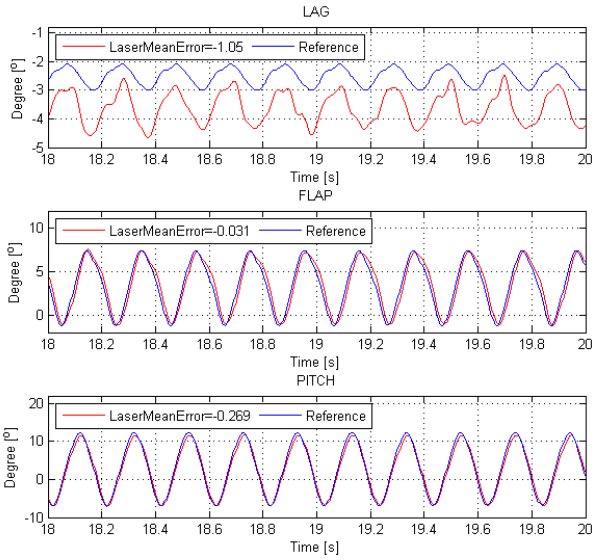

(a) airspeed = v_1

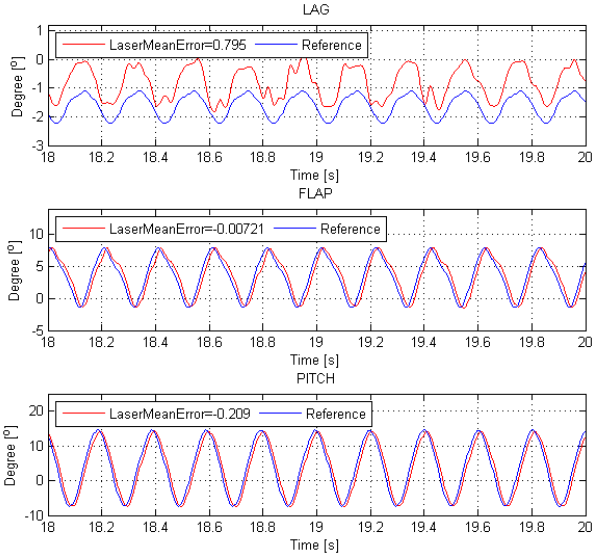

(b) airspeed = v_2

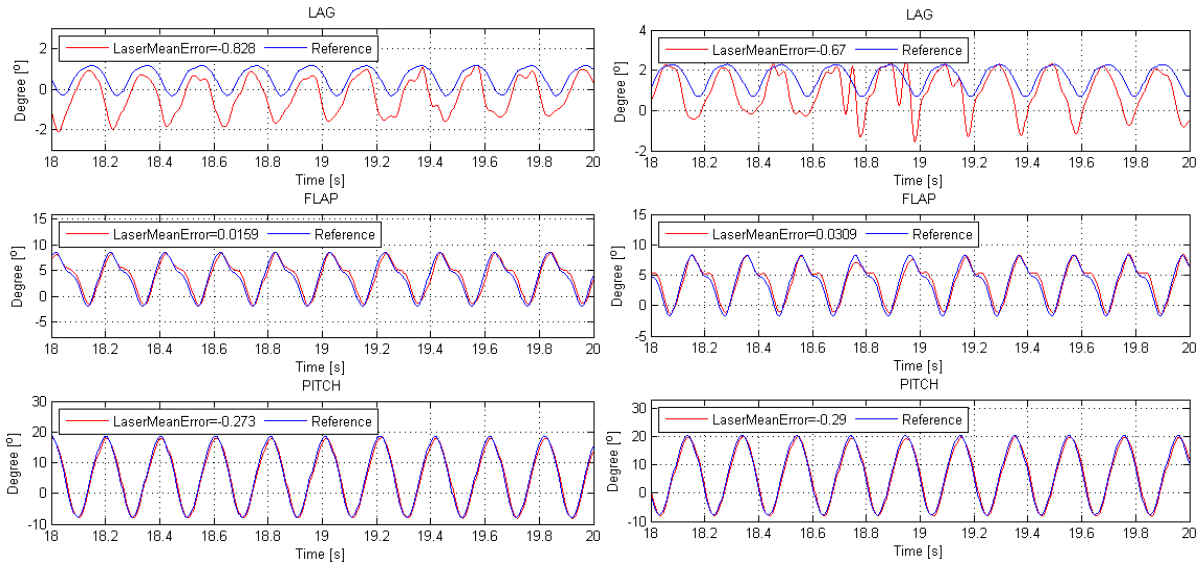

(c) airspeed = v_3 (d) airspeed = v_4

Figure 11: Blade angles estimated with the 2D laser triangulation systems in realistic conditions with different simulated airspeed values: (a) airspeed = v_1; (b) airspeed = v_2; (c) airspeed = v_3; (d) airspeed = v_4.

Note that, in the case of high-amplitude pitch angle, the profile in Figure 3c is rotated in the X_L-Y_L plane with large amplitudes; in these conditions the laser sensor does not provide correct measurement of the blade angles, as can be seen in Figure 12a, where large spikes in laser data correspond to wrong measured angles. This is mainly due to the fact that, as the pitch angle increases, there is a high risk of disappearance of the points at the valleys (P_{L1}, P_{L4}, P_{L6} and P_{L9}) in the measured profile, due to the undercuts (see Figure 12b). Considering that the motion of the blade root depends on the lag, flap and pitch angles, the problem of undercuts can happen for different blade angles combinations. The points P_{L2}, P_{L3}, P_{L5}, P_{L7} and P_{L8} are always visible to the laser (and therefore correctly measured) while the other points can be not visible in some blade attitudes, preventing the possibility to estimate the blade angles using the 2D laser. This problem can be mitigated by adjusting the profile of the target, but this may result in an increase of the measuring uncertainty. In particular, because of the working principle of the laser system, reducing the height of the profile of the target decreases the risk of undercuts, but produces a proportional increase in the uncertainty of the measurements. This is because the lower is the height of the profile of the target, the worse is the signal-to-noise ratio in the detection of the corners of the target, and this has a direct effect on measurement uncertainty.

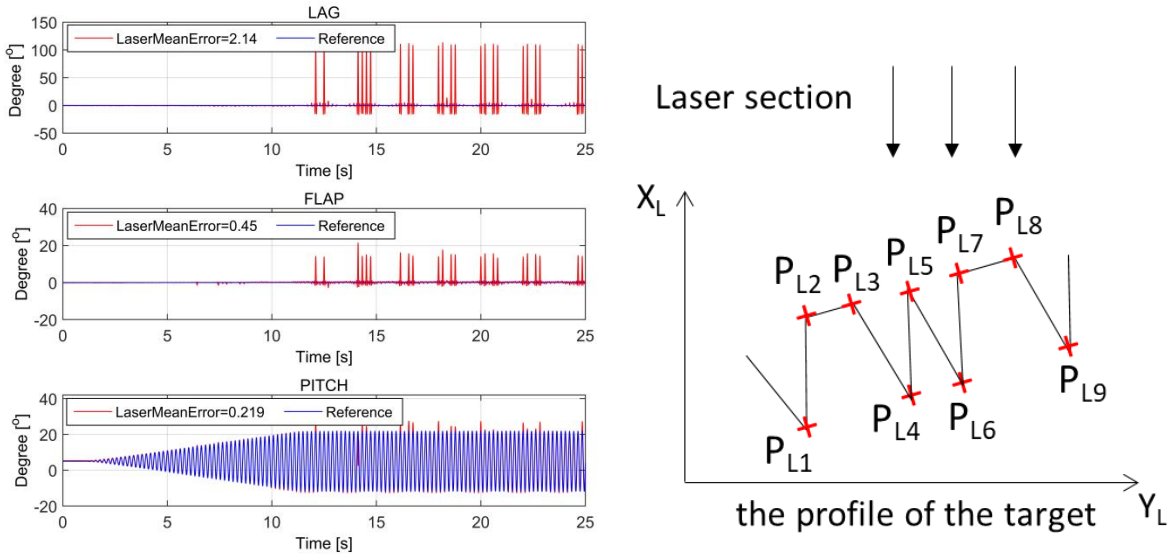

(a) (b)

Figure 12: (a) Blade angles estimated by means of 2D laser system in the case of large pitch angle (from -5° to 17°). (b) the profile of the target in case of pure big pitch

4.3 Accuracy tests: Vision systems

Both the measuring systems based on single camera and stereoscopic cameras were mounted together on the AW139 endurance rig: in this way, the two systems were tested simultaneously, with the same reference data. In this section, the results obtained with the two types of vision-based systems are shown together, to facilitate the comparison.

Figure 13 shows one segment of the time histories of lag/flap/pitch angles: the blue curve represents the reference data, the green curve represents the angles estimated with the single camera system and the red curve represents the angles estimated with the stereo camera system. A detailed comparison between the different solutions is given in section 4.3.4. However, it is apparent that the overall agreement of the two vision systems with the reference data is better than the case of 2D laser solution. Moreover, even in the case of very large pitch angles (where the laser solution failed), both the vision-based solutions measured the three angles correctly, as it can be seen in Figure 14.

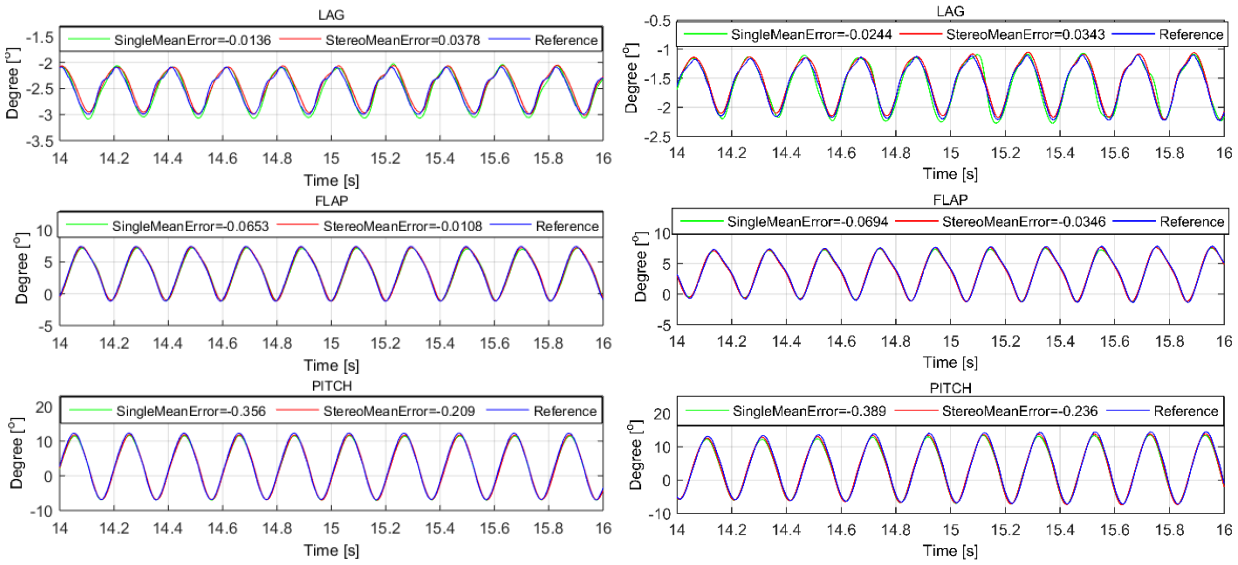

(a) airspeed = v_1 (b) airspeed = v_2

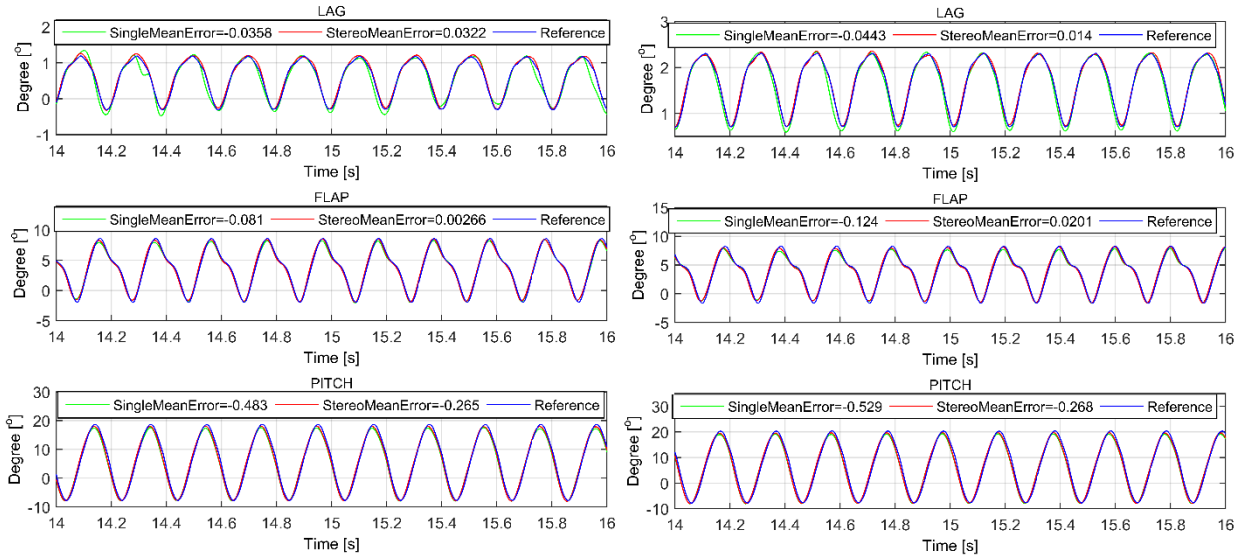

(c) airspeed = v_3 (d) airspeed = v_4

Figure 13: Blade angles estimated with the vision-based systems in realistic conditions with different simulated airspeed values: (a) airspeed = v_1; (b) airspeed = v_2; (c) airspeed = v_3; (d) airspeed = v_4.

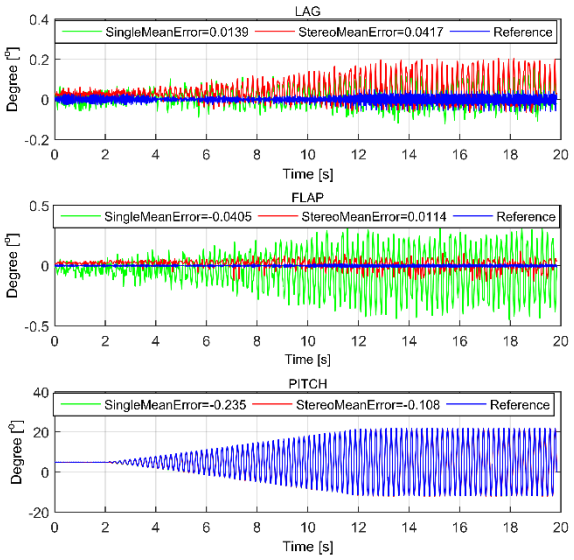

Figure 14: Blade angles estimated by means of vision-based systems in the case of large pitch angle (from -5° to 17°).

4.4 Accuracy tests: Comparison among the three systems

The discrepancies between the reference values and the angles estimated with the three developed systems are analyzed here, in order to compare the three solutions in terms of measuring accuracy. Note that the acquisition frequencies (40 Hz for the laser system and 35 Hz for the vision system) are different from the 247 Hz frequency of the reference system. Therefore, the data from the three developed systems have been resampled at 247 Hz and synchronized with the reference measurement. Then, the time history of the discrepancy is computed for the three blade angles. The discrepancies are then processed to extract, for each blade angle, the mean discrepancy and the discrepancy on the first three harmonic components. Finally, the average value of the discrepancy is considered as the characteristic discrepancy of the angle measurement.

Figure 15 shows the discrepancies between the blade angles measured by means of the three developed systems and the reference values, for the four different airspeed conditions. For the laser system, the discrepancy of the lag angle is approximately 1°, while the discrepancy of the flap angle is below 0.1° and the discrepancy of the pitch angle is below 0.3°. The high discrepancy for the lag angle is likely due to the complex calibration procedure: multiple parameters of the calibration target are required due to the intrinsic principle of the laser system in order to recover the roto-translation of the target. Moreover, the calibration procedure assumes that the X_LZ_L plane is overlapped with the X_fZ_f plane. However, in actual implementation, the laser sensor position can be biased by a small rotation around the Z_f direction, representing a lag displacement.

For the vision system, the measurement of the lag angle and the flap angle displays a very high accuracy, which is always below 0.15°. The measurement of the pitch angle shows the biggest discrepancy among these three angles, in both of the vision systems. As expected, the discrepancy of the pitch angle for the single camera is always higher than that for the stereo camera system. This is because only four blobs are applied to estimate the three angles for the single camera, instead of eight blobs for the stereo camera system. Since the inverse problem of recovering the angles is overconditioned, overabundant data can help to improve accuracy. Note that for the single camera system, the maximum discrepancy of the pitch angle in these cases is around 0.5°, which can be judged acceptable for the target application. The stereo

camera system has a better accuracy. Even in the worst conditions (v_4), the discrepancy of the pitch angle is still below 0.3°. It is possible to further improve the accuracy of the pitch angle by means of increasing the distance between the blobs in the target pattern. However, as the distance between the blobs is increased, the risk of the disappearance of a blob is increased, because of the limitation of the field of view and the large motion of the blade.

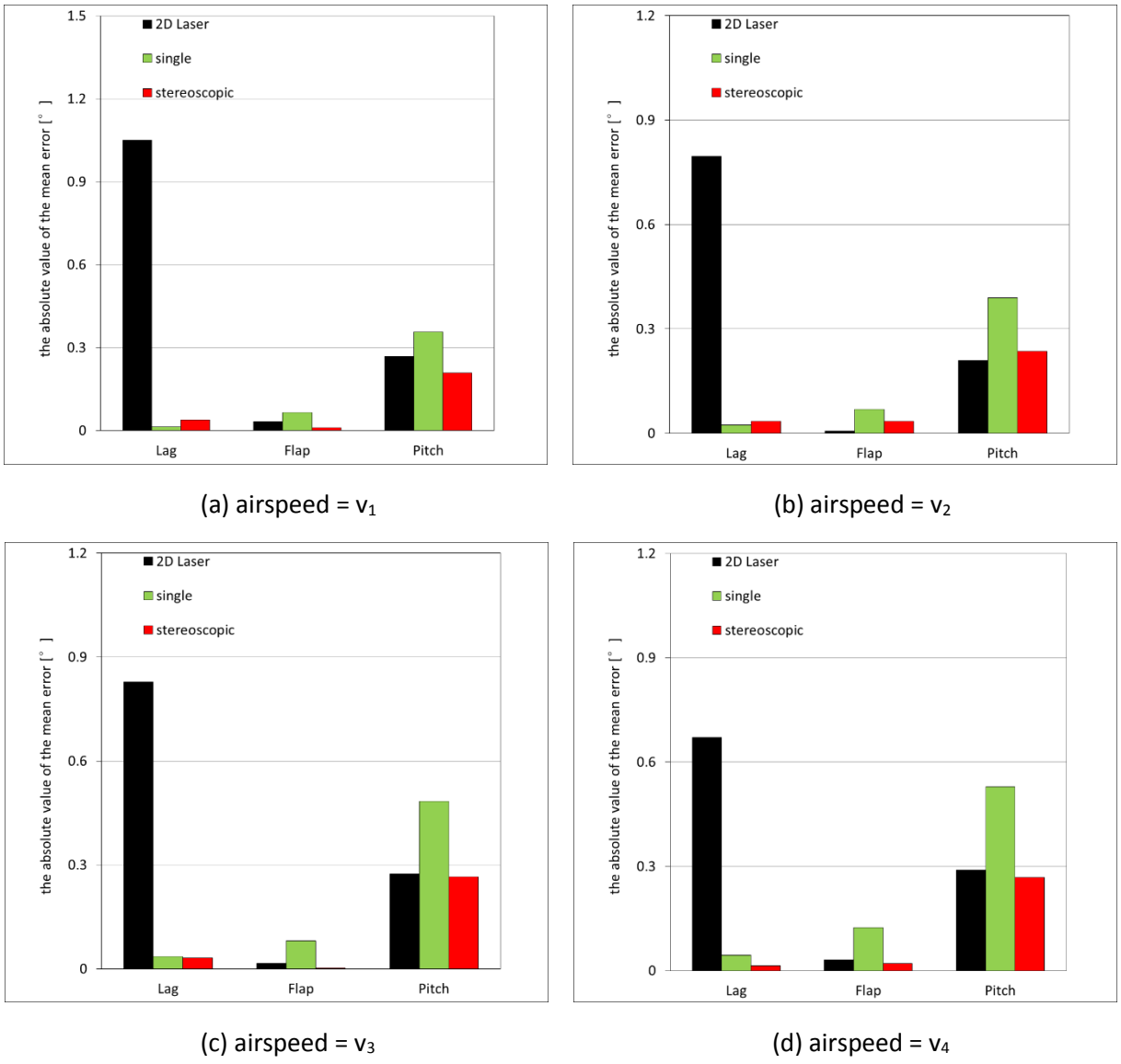

Figure 15: Discrepancy of the mean value of lag-flap-pitch angles by means of the three systems in case of different airspeed conditions: (a) airspeed = v_1; (b) airspeed = v_2; (c) airspeed = v_3; (d) airspeed = v_4.

The results for the amplitude of the 1st harmonic at 4.94 Hz of the three angles for the three systems have also been evaluated. We remark that the 1st harmonic motion, and particularly cyclic flapping, is highly meaningful for noise reduction applications, as it can be correlated with the tip-path plane angle of attack, which is a fundamental driver of the rotor acoustic emission.

As Figure 16 shows, also the stereo camera system presents remarkably better performance than the laser system and the single camera system. The laser system retains the worst accuracy for the lag angle.

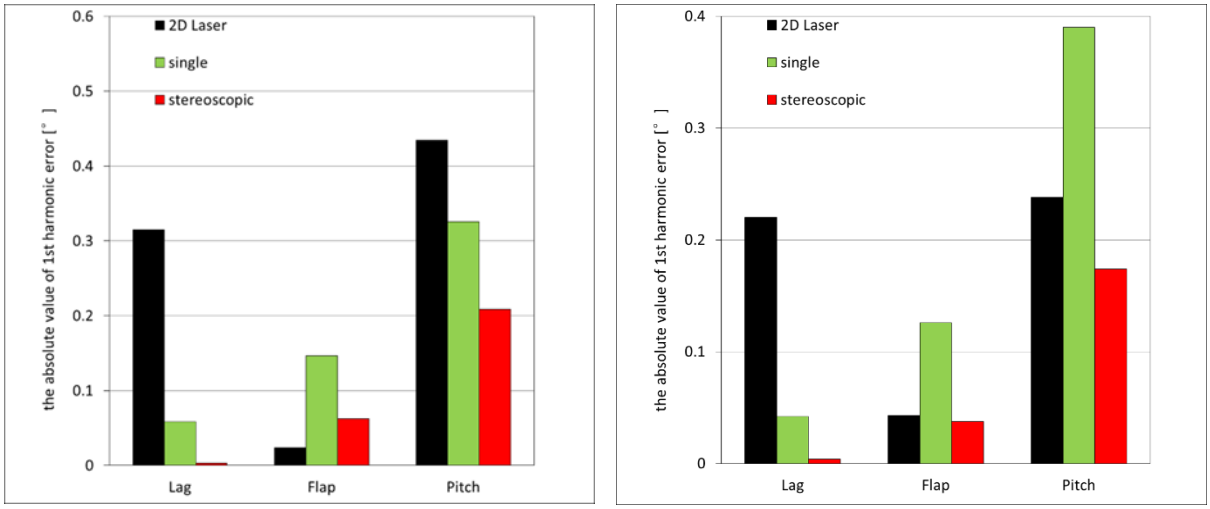

(a) airspeed = v_1 (b) airspeed = v_2

(c) airspeed = v_3 (d) airspeed = v_4

Figure 16: Discrepancy of 1st harmonic of lag-flap-pitch angles by means of the three systems in case of different airspeed conditions: (a) airspeed = v_1; (b) airspeed = v_2; (c) airspeed = v_3; (d) airspeed = v_4.

In addition, 2nd harmonic and 3rd harmonic components have been considered too. The related amplitudes for three angles are clearly far lower than those characterizing the 1st harmonic. Generally, the discrepancies of the two harmonics for the three systems have a similar order of magnitude. For the stereo camera system, the absolute value of the discrepancy of these higher harmonics is lower than 0.1°.

5 Conclusion

The measurement of helicopter main rotor tip-path plane orientation with respect to the fuselage is a key factor when approaching emitted noise reduction through in-flight trajectories optimization, as envisaged in the MANOEUVRES project. A fundamental ingredient is thus the real-time measurement of the blade attitude, in order to feed a complex system capable to deliver noise footprint information to the pilot [4]. A blade motion sensor may also be used in further applications, including advanced health monitoring, system identification, and flight control augmentation **Errore. L'origine riferimento non è stata trovata.**.

Currently, mechanical sensors capable of acquiring the coupled blade motion exist, but are usually limited to experimental activities, due to their low reliability and durability. Thus, a novel measurement system architecture, based on contactless sensors, has been conceived, developed and tested in this work. Main rotor blade attitude can be estimated relying on the time histories of the three blade angles, therefore the focus of this work is on sensor systems for blade angle estimation.

After a preliminary analysis that considered a wide variety of possible technologies, three novel contactless measurement systems, have been designed and developed. These are based on 2D laser triangulation, single camera and stereo cameras, respectively. The three systems have been applied to reconstruct the spatial position of appropriate features positioned on the blade root. Relying on these positions, the blade angles are recovered. Although all the developed solutions are based on the principle of detecting and processing the 3D position of features on the blade root, this goal is obtained with a completely different approach in each solution. The principles of operation of the three measuring solutions, as well as the main implementation details have been described in the paper. For each measuring solution, specialized algorithms have been developed for the system calibration and for the real-time angle recovery.

In order to evaluate the most promising solution, an experimental campaign was carried out on full-scale prototypal realizations of the three systems. This campaign involved test rigs at both the Politecnico di Milano laboratories and Leonardo Helicopters, and was structured on three types of tests aimed at the verification of the transducer functionality and actual capability. All the three systems passed the vibration test and the coupled rotation and vibration test successfully, therefore, in terms of mechanical resistance, no evident differences arose among the three solutions. The maximum sampling frequency was 40Hz for the laser-based solution and 35Hz for the vision-based ones, therefore, all the solutions ensured the frequency bandwidth of 15Hz required for this application, in order to correctly estimate the tip-path-plane. Moreover, the maximum allowed mass for the measuring system was fixed by Leonardo Helicopters to 4.5kg. All the proposed measuring devices respected this limit. Other factors, such as, cost index, technical challenge, technical capability, and road to commercial exploitation of each solution were analyzed in an earlier work, where it was shown that the key parameter for the selection of the final solution is the measuring accuracy [43]. Thanks to the extensive qualification work described in sections 3 and 4 of this work, it was finally possible to select the stereoscopic vision system as the most appropriate measuring solution for the application considered in the MANOEUVRES project. Indeed, the comparison between the results of the stereoscopic vision system and the reference angles (provided by the instrumentation of the AW139 endurance rig at the Leonardo Helicopters laboratories) showed discrepancies for lag, flap and pitch angle below 0.1^{o}, 0.1^{o} and 0.3^{o} respectively in case of realistic blade motion condition, i.e. an accuracy achieving the requirement considered for helicopter noise prediction applications.

Acknowledgements

The authors acknowledge the financial support by the MANOEUVRES project, framed within the Green RotorCraft (GRC) Integrated Technology Demonstrator of the European Union Clean Sky Joint Technology Initiative under Grant Agreement N. 620068.

References

[1] M.D. Takahashi, Rotor-state feedback in the design of flight control laws for a hovering helicopter, J. Am. Helicopter Soc. 39 (1994) 50–62.

[2] C.M. Ivler, Development and comparison of explicit and implicit rotor-state feedback control systems for a Fly-by-Wire UH-60, AHS Rotorcraft Handling Qualities Specialists' Meeting, Huntsville, U.S.A., February, 2014.

[3] P. Cordisco, R. Liu, M. Redaelli, et al., Developing a novel contactless sensor for helicopter rotor state measurements, 36th European Telemetry and Test Conference ETC2016 - 3rd Symposium on Advanced In-flight Measurement Techniques AIM2016, Nuremberg, Germany, May, 2016.

[4] L. Trainelli, M. Gennaretti, G. Bernardini, et al., Innovative helicopter in-flight noise monitoring enabled by rotor state measurements, Noise Mapping, 3 (1) (2016) 190-215.

[5] D.A. Barrows, A.W. Burner, A.I. Abrego, et al., Blade displacement measurements of the full-scale UH-60A airloads rotor, 29th AIAA Applied Aerodynamics Conference, Hawaii, U.S.A., June, 2011.

[6] S. Panza, M. Lovera, Rotor state feedback in helicopter flight control: robustness and fault tolerance, 2014 IEEE Conference on Control Applications (CCA) Part of 2014 IEEE Multi-conference on Systems and Control, Antibes, France, October, 2014.

[7] A.I. Abrego, L.E. Olson, E.A. Romander, et al., Blade displacement measurement technique applied to a full-scale rotor test, American Helicopter Society 68th Annual Forum, Texas, U.S.A., May, 2012.

[8] J.F. Horn, W. Guo, G.T. Ozdemir, Use of rotor state feedback to improve closed-loop stability and handling qualities, J. Am. Helicopter Soc. 57 (2012) 1-10.

[9] L. Trainelli, M. Lovera, A. Rolando, et al., Project MANOEUVRES – towards real-time noise monitoring and enhanced rotorcraft handling based on rotor state measurements, 41st European Rotorcraft Forum ERF 2015, Munich, Germany, September 1-4, 2015.

[10] W. Johnson, A history of rotorcraft comprehensive analyses, American Helicopter Society 69th Annual Forum, Phoenix, Arizona, U.S.A, May, 2013.

[11] S. Ananthan, J.G. Leishman, Transient helicopter rotor wakes in response to time-dependent blade pitch inputs, Journal of Aircraft, 41 (5) (2004) 1025-1041.

[12] V.H. Knight, W.S. Haywood, M.L. Williams, A rotor-mounted digital instrumentation system for helicopter blade flight research measurements, NASA Technical Paper 1146, 19780012185, 1978.

[13] C. Perrin, N. Imbert, C. Chuc, Device for monitoring the flapping and/or lag behavior of a blade of a rotorcraft rotor, United States Patent, No. US 20130243597 A1, 2013.

[14] S.A. Jacklin, A. Haber, G. de Simone, T.R. Norman, et al., Full-scale wind tunnel test of an individual blade control system for a UH-60 helicopter, American Helicopter Society 58th Annual Forum, Montreal, Canada, June, 2002.

[15] R.M. Kufeld, D.L. Balough, J.L. Cross, et al., Flight testing the UH-60A airloads aircraft, American Helicopter Society 50th Annual Forum, Washington DC, U.S.A., May, 1994.

[16] D. Marioli, E. Sardini, A. Taroni, Ultrasonic distance measurement for linear and angular position control, IEEE T. Instrum. Meas., 37(4) (1988) 578-581.

[17] T. Yata, L. Kleeman, S. Yuta, Wall following using angle information measured by a single ultrasonic transducer, Proceedings of the 1998 IEEE international conference on robotics and automation, Leuven, Belgium, May, 1998, pp. 1590-1596.

[18] S. Shoval, J. Borenstein, Measurement of angular position of a mobile robot using ultrasonic sensors, ANS conference on robotics and remote Systems, Pittsburgh, PA, U.S.A., April, 1999.

[19] P.L. Fulmek, F. Wandling, W. Zdiarsky, et al., Capacitive censor for relative angle measurement, IEEE IEEE T. Instrum. Meas., 51(6) (2002) 1145-1149.
[20] M. Gasulla, X. Li, G.C.M. Meijer, et al., A contactless capacitive angular-position Sensor, IEEE Sensors Journal, 3(5) (2003) 607- 614.
[21] M. Fontana, F. Salsedo, M. Bergamasco, Novel magnetic sensing approach with improved linearity, Sensors, 13(6) 2013 7618-7632.
[22] C. Mandache, T. Mcelhinney, N. Mrad, Aircraft engine blade tip monitoring using pulsed eddy current technology, 4th International Symposium on NDT in Aerospace, Augsburg, German, November, 2012.
[23] Y. Lai, Eddy current displacement sensor with LTCC technology, doctor dissertation, Albert-Ludwigs University of Freiburg, 2005.
[24] T.C. Schank, Rotor position determination system with Hall-effect sensors, United States Patent, No. US 20140061369 A1, 2014.
[25] A. Buschbaum, V. Plassmeier, Angle measurement with a Hall Effect sensor, Smart Mater. Struct., 16 (2007) 1120-1124.
[26] K.V. Dimitrov, A 3-D Hall sensor for precise angular position measurements, Turk. J. Phys, 31 (2007) 97-101.
[27] Z. Zhang, Q. Feng, Z. Gao, et al., A new laser displacement sensor based on triangulation for gauge real-time measurement, Opt. Laser Technol., 40 (2008) 252-255.
[28] Y. Ma, S. Soatto, J. Kosecka et al., An Invitation to 3-D Vision, Springer New York, 2004 (Chapter 3 and 6).
[29] J.W. Fletcher, M.B. Tischler, Improving helicopter flight mechanics models with laser measurements of blade flapping, American Helicopter Society 53rd Annual Forum, Virginin, U.S.A., April, 1997.
[30] R. Sickenberger, An image-based approach for tracking helicopter longitudinal tip-path-plane angle, master dissertation, University of Maryland, U.S.A., 2008.
[31] C.M. Ferrar, R. Zincone, Optical position and orientation sensing systems, United States Patent, No. US 4583862 A, 1986.
[32] S. Kumar, P.K. Tiwari, S.B. Chaudhury, An optical triangulation method for non-contact profile measurement, IEEE international conference on industrial technology, Mumbai, India, December, 2006.
[33] G.C. Myers, Flight measurements of helicopter blade motion with a comparison between theoretical and experimental results, National Advisory Committee for Aeronautics Technical Note No. 1266, 1947.
[34] G.A. Brés, K.S. Brentner, G. Perez, et al., Maneuvering rotorcraft noise prediction, Sound Vib., 275 (2004) 719-738.
[35] M. Gennaretti, J. Serafini, G. Bernardini, et al., Numerical characterization of helicopter noise hemispheres, Aerospace Sci. Technol., 52 (2016) 18-28.
[36] D. Peng, Y. Liu, A grid-pattern PSP/TSP system for simultaneous pressure and temperature measurements, Sensor. Actuat. B-Chem., 222 (2016) 141-150.
[37] D. Peng, L. Jiao, Y. Liu, Development of a grid PSP/TSP system for unsteady measurements on rotating surfaces, 32nd AIAA Aerodynamic Measurement Technology and Ground Testing Conference, Washington, D. C., U.S.A., June, 2016.
[38] R. W. Farebrother, Fitting linear relationships: a history of the calculus of observations 1750-1900, Springer New York, 1999 (Chapter 5).

[39] J.C.A. Barata, M.S. Hussein, The Moore-Penrose pseudoinverse: a tutorial review of The theory, Braz. J. Phys., 42 (2012) 146-165.
[40] J. Didier, F. Ababsa, M. Mallem, Hybrid camera pose estimation combining square fiducials localization technique and orthogonal iteration algorithm, Int. J. Image Grap., 8 (1) (2008) 169-188.
[41] R.I. Hartley, P. Sturm, Triangulation, Comput. Vis. Image Und., 68(2) (1997) 146-157.
[42] G.L. Ghiringhelli, M. Terraneo, E. Vigoni, Improvement of structures vibroacoustics by widespread embodiment of viscoelastic materials, Aerospace Sci. Technol., 28 (2013) 227-241.
[43] A. Cigada, A. Colombo, P. Cordisco, et al., Contactless rotor flapping sensor design, implementation and testing, American Helicopter Society 72nd Annual Forum, U.S.A., May, 2016.